Ground state phase diagram of the Kitaev-Heisenberg model on a honeycomb-triangular lattice

Masanori Kishimoto,[1,*] Katsuhiro Morita,[1,†] Yukihiro Matsubayashi,[1] Shigetoshi Sota,[2] Seiji Yunoki,[2,3,4] and Takami Tohyama[1]

[1]*Department of Applied Physics, Tokyo University of Science, Tokyo 125-8585, Japan*
[2]*Computational Materials Science Research Team, RIKEN Center for Computational Science, Kobe, Hyogo 650-0047, Japan*
[3]*Computational Condensed Matter Physics Laboratory, RIKEN, Wako, Saitama 351-0198, Japan*
[4]*Computational Quantum Matter Research Team, RIKEN Center for Emergent Matter Science, Wako, Saitama 351-0198, Japan*

(Received 17 April 2018; revised manuscript received 16 July 2018; published 10 August 2018)

The Kitaev-Heisenberg model defined on both honeycomb and triangular lattices has been studied intensively in recent years as a possible model to describe spin-orbital physics in iridium oxides. In the model, there are many phases characteristic for each lattice. However, there is no study of how the phases in the two lattices merge with each other when geometry changes from the honeycomb lattice to triangular lattice. We investigate the ground state of the Kitaev-Heisenberg model defined on the system connecting the honeycomb and triangular lattices, named a honeycomb-triangular lattice. We obtain a ground state phase diagram of this model with classical spins by using the Luttinger-Tisza method and classical Monte Carlo simulation. In addition to known phases in the honeycomb and triangular lattices, we find coexisting phases consisting of the known phases. From the exact diagonalization and density-matrix renormalization-group calculations for the model with quantum spins, we find phases similar to the classical results, implying a small effect of quantum fluctuation on the phase diagram.

DOI: 10.1103/PhysRevB.98.054411

I. INTRODUCTION

Strong spin-orbital interaction plays an important role in iridium oxides by entangling spin and orbital degrees of freedom in $5d$ electrons. As a result, the iridates can be effectively described by Kitaev-type interactions together with isotropic Heisenberg-type interactions [1]. When the Kitaev interactions, which were originally studied by Kugel and Khomskii on the basis of the compass model [2–4], dominate on a honeycomb lattice, a Kitaev spin liquid appears [5]. This fact has brought about intensive studies of the Kitaev-Heisenberg (KH) model on the honeycomb lattice, which is expected to be an effective model for $(\mathrm{Na, Li})_2\mathrm{IrO}_3$ [6–13]. To describe $(\mathrm{Na, Li})_2\mathrm{IrO}_3$ more realistically, extended versions of the KH model with further-neighbor interactions [14–17] and additional anisotropic interactions [18–27] have been studied.

In addition to the honeycomb lattice, the KH model on a triangular lattice has attracted attention from a theoretical viewpoint [28–32] since it has both geometrical frustration and Kitaev-type frustration that breaks the SU(2) spin symmetry. In addition, from the experimental side, $\mathrm{Ba_3IrTi_2O_9}$ has been suggested as a possible spin-liquid material with a frustrated triangular-lattice structure containing compasslike magnetic interactions [33,34] and has been discussed in connection to the KH model [35].

Although the KH model cannot properly describe existing iridates, the model has attracted a lot of attention in terms of phase diagrams on the honeycomb lattice [6,7,10] and the triangular lattice [28–30,32]. In the honeycomb lattice, there are the Néel, spin-liquid, zigzag, ferromagnetic (FM), and stripy phases, while in the triangular lattice there are the 120° ordered, $\mathbb{Z}_2$ vortex crystal ($\mathbb{Z}_2$VC), nematic, dual-$\mathbb{Z}_2$VC, and dual-FM phases. These phases appearing in the two lattices are not the same. It is thus interesting to know how the phases evolve and merge with each other when geometry changes from honeycomb lattice to triangular lattice. This connection of the two lattices will contribute to searching for new phases in the KH model. From the experimental side, there is no material described by the connected model at present. However, we expect that such materials will be synthesized in the near future, for example, by distorting the lattice or replacing ions with others in the honeycomb and triangular lattices described by the KH model. Therefore, the connection of the two lattices will bring new views in the study of the KH model.

In this paper, we construct a model connecting the honeycomb and triangular KH lattices and examine the ground state of the classical system using the Luttinger-Tisza (LT) method [36,37] and the classical Monte Carlo (MC) simulation. We find coexisting phases in the honeycomb-triangular lattice which are composed of the known phases. The phase boundaries in the classical phases survive even though quantum fluctuations are introduced as evidenced by the exact-diagonalization (ED) and density-matrix renormalization-group (DMRG) calculations for small systems.

This paper is organized as follows. The KH model on the honeycomb-triangular lattice is introduced in Sec. II. In Sec. III, the methods used in this paper, i.e., the LT method, classical MC simulation, ED, and DMRG, are described. The classical ground state phase diagram is shown in Sec. IV, with the emphasis on the nature of coexisting phases. In Sec. V, we examine the ground state of the same model for quantum spins

*1517611@ed.tus.ac.jp
†katsuhiro.morita@rs.tus.ac.jp

 ©2018 American Physical Society

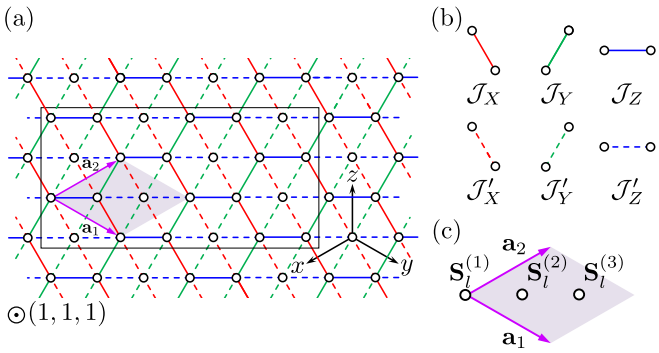

FIG. 1. (a) Honeycomb-triangular lattice on the plane perpendicular to $(x, y, z) = (1, 1, 1)$, where (x, y, z) is the orthogonal coordinate system used for the spin space. The red, green, and blue lines are perpendicular to the x, y, and z axes, respectively. The solid lines form the honeycomb lattice, while the dashed lines connect the honeycomb sites with a central site. The shaded area represents a unit cell. The rectangle denoted by black solid lines presents a 24-site lattice with eight unit cells used in ED calculations. (b) Six types of nearest-neighbor interactions appearing in (a). The red solid, green solid, blue solid, red dashed, green dashed, and blue dashed lines represent the matrices of nearest-neighbor interactions, $\mathcal{J}_X$, $\mathcal{J}_Y$, $\mathcal{J}_Z$, $\mathcal{J}'_X$, $\mathcal{J}'_Y$, and $\mathcal{J}'_Z$, respectively. The matrices of the interactions contain only diagonal elements (see the main text). (c) The definition of unit cell. $\mathbf{a}_1$ and $\mathbf{a}_2$ are two primitive translation vectors. $\mathbf{S}_l^{(m)}$ represents a spin at the sublattice m in the unit cell l.

using the ED and DMRG methods and show a quantum phase diagram. Finally, a summary is given in Sec. VI.

II. MODEL

The Hamiltonian of the Kitaev-Heisenberg model on the honeycomb-triangular lattice is given by

$$\mathcal{H} = \sum_{\langle i,j \rangle} \mathbf{S}_i^{\mathrm{T}} \mathcal{J}_{i,j} \mathbf{S}_j, \tag{1}$$

where $\mathbf{S}_i$ is a classical spin $\mathbf{S}_i = (S_i^x \ S_i^y \ S_i^z)^{\mathrm{T}} \in \mathbb{R}^3$ with $|\mathbf{S}_i| = 1$ (a spin operator with $S = 1/2$) at site i for the classical (quantum) system. $\mathcal{J}_{i,j}$ represents the nearest-neighbor interaction given by the matrix form: for the bond connecting two honeycomb sites, $\mathcal{J}_X$, $\mathcal{J}_Y$, and $\mathcal{J}_Z$ are perpendicular to the x, y, and z directions in the spin space, respectively, while for the bond connecting a honeycomb site to a neighboring central site, $\mathcal{J}'_X$, $\mathcal{J}'_Y$, and $\mathcal{J}'_Z$, are assigned, as shown in Figs. 1(a) and 1(b). All of the matrices have only diagonal elements with $\mathcal{J}_X = \mathrm{diag}(J + K, J, J)$, $\mathcal{J}_Y = \mathrm{diag}(J, J + K, J)$, $\mathcal{J}_Z = \mathrm{diag}(J, J, J + K)$, $\mathcal{J}'_X = \alpha\mathcal{J}_X$, $\mathcal{J}'_Y = \alpha\mathcal{J}_Y$, and $\mathcal{J}'_Z = \alpha\mathcal{J}_Z$ $(0 < \alpha \leqslant 1)$, where K and J correspond to the coefficient of the Kitaev and Heisenberg terms, respectively. The parameter α determines how close a given lattice is to the triangular lattice; that is, $\alpha = 1$ corresponds to a triangular lattice, while $\alpha \to 0^+$ corresponds to a honeycomb lattice. We note that there is Klein duality [28] in this model, which transforms $(J, K) \mapsto (\tilde{J}, \tilde{K}) = (-J, 2J + K)$.

III. METHOD

A. Luttinger-Tisza method

In order to analyze the classical ground state, we introduce a unit cell as shown in Fig. 1(c) and the Fourier transform of spins defined as

$$S_l^{(m)\gamma} \equiv \frac{1}{\sqrt{N}} \sum_{\mathbf{q}} e^{i\mathbf{q}\cdot\mathbf{r}_l^{(m)}} S_{\mathbf{q}}^{(m)\gamma}, \tag{2}$$

where $S_l^{(m)\gamma}$ denotes the γ component of the spin $\mathbf{S}_l^{(m)}$ at $\mathbf{r}_l^{(m)}$ belonging to sublattice m in unit cell l and N is the number of unit cells. From Eqs. (1) and (2), the total energy of the system is given by

$$E_{\mathrm{tot}} = \frac{1}{2} \sum_{\gamma\in\{x,y,z\}} \sum_{\mathbf{q}\in V_{\mathrm{BZ}}} \mathbf{S}_{-\mathbf{q}}^{\gamma\mathrm{T}} \mathcal{J}_{\mathbf{q}}^{\gamma} \mathbf{S}_{\mathbf{q}}^{\gamma}, \tag{3}$$

where the summation $\sum_{\mathbf{q}\in V_{\mathrm{BZ}}}$ is taken over the wave vectors in the first Brillouin zone V_{BZ}. The three-dimensional vector $\mathbf{S}_{\mathbf{q}}^{\gamma}$ is defined as $\mathbf{S}_{\mathbf{q}}^{\gamma} \equiv (S_{\mathbf{q}}^{(1)\gamma} \ S_{\mathbf{q}}^{(2)\gamma} \ S_{\mathbf{q}}^{(3)\gamma})^{\mathrm{T}}$, and the Fourier transform of the interaction is given by

$$\mathcal{J}_{\mathbf{q}}^{\gamma} = \begin{pmatrix} 0 & A_{\mathbf{q}}^{\gamma} & \alpha A_{\mathbf{q}}^{\gamma *} \\ A_{\mathbf{q}}^{\gamma *} & 0 & \alpha A_{\mathbf{q}}^{\gamma} \\ \alpha A_{\mathbf{q}}^{\gamma} & \alpha A_{\mathbf{q}}^{\gamma *} & 0 \end{pmatrix}, \tag{4}$$

with

$$\begin{aligned} A_{\mathbf{q}}^{x} &= (J + K) e^{i\frac{2\pi}{3}(-2m_1+m_2)} + J e^{i\frac{2\pi}{3}(m_1-2m_2)} \\ &\quad + J e^{i\frac{2\pi}{3}(m_1+m_2)}, \\ A_{\mathbf{q}}^{y} &= J e^{i\frac{2\pi}{3}(-2m_1+m_2)} + (J + K) e^{i\frac{2\pi}{3}(m_1-2m_2)} \\ &\quad + J e^{i\frac{2\pi}{3}(m_1+m_2)}, \\ A_{\mathbf{q}}^{z} &= J e^{i\frac{2\pi}{3}(-2m_1+m_2)} + J e^{i\frac{2\pi}{3}(m_1-2m_2)} \\ &\quad + (J + K) e^{i\frac{2\pi}{3}(m_1+m_2)}, \end{aligned}$$

where m_1 and m_2 are integers that specify the wave vector as $\mathbf{q} = m_1\mathbf{b}_1 + m_2\mathbf{b}_2$, with $\mathbf{b}_1$ and $\mathbf{b}_2$ being the reciprocal lattice vectors.

To find the ground state, we need to minimize E_{tot} with respect to $\{\mathbf{S}_{\mathbf{q}}^{\gamma}\}$ under the local constraints:

$$\left|\mathbf{S}_l^{(m)}\right|^2 = 1 \quad (l = 1, 2, \ldots, N;\ m = 1, 2, 3). \tag{5}$$

The LT method [36,37] is useful for such a minimization problem. The local constraint is often replaced by the single global constraint $\sum_{l,m} |\mathbf{S}_l^{(m)}|^2 = 3N$. However, this approach generally fails when the unit cell contains nonequivalent sites like the present model (1). Therefore, we consider minimizing E_{tot} under the improved global constraints [37–39]:

$$\sum_{l=1}^{N} \left(\left|\mathbf{S}_l^{(1)}\right|^2 + \left|\mathbf{S}_l^{(2)}\right|^2\right) = 2N, \quad \sum_{l=1}^{N} \left|\mathbf{S}_l^{(3)}\right|^2 = N. \tag{6}$$

Assuming that $\mathbf{S}_{\mathbf{q}}^{\gamma}$ has finite magnitude, we obtain the energy per unit cell

$$E_{\mathrm{unit}} = \frac{1}{2}\left[3\lambda - (1 - \alpha^2)\frac{\left|A_{\mathbf{q}}^{\gamma}\right|^2}{\lambda}\right], \tag{7}$$

where λ is obtained as the solution of the following equation:

$$\lambda^4-(\alpha^2+2)\left|A_{\mathbf{q}}^{\gamma}\right|^2\lambda^2-2\alpha^2\mathrm{Re}\left[A_{\mathbf{q}}^{\gamma 3}\right]\lambda+(1-\alpha^2)\left|A_{\mathbf{q}}^{\gamma}\right|^4=0. \tag{8}$$

Thus, we need to find $\{(\mathbf{q}',\gamma')\}$ ($\subset V_{\mathrm{BZ}}\times\{x,y,z\}$) whose elements give the same λ, minimizing E_{unit}. For $(\mathbf{q},\gamma)\notin\{(\mathbf{q}',\gamma')\}$, $\mathbf{S}_{\mathbf{q}}^{\gamma}$ has no magnitude, while for $(\mathbf{q},\gamma)\in\{(\mathbf{q}',\gamma')\}$, $\mathbf{S}_{\mathbf{q}}^{\gamma}$ satisfies

$$\mathcal{J}_{\mathbf{q}}^{\gamma}\mathbf{S}_{\mathbf{q}}^{\gamma}=\Lambda\mathbf{S}_{\mathbf{q}}^{\gamma}, \tag{9}$$

with

$$\Lambda\equiv\mathrm{diag}(\lambda,\lambda,2(E_{\mathrm{unit}}-\lambda)). \tag{10}$$

When this solution satisfies the local constraints (5), it is the ground state.

We numerically solve Eq. (8) to find $\{(\mathbf{q}',\gamma')\}$. However, since the local constraints (5) are not necessarily satisfied when $\mathbf{q}'$ is incommensurate to the lattice, we use the classical MC simulation for such cases.

B. Classical Monte Carlo simulation

Our classical MC simulation is based on the single-update heat-bath method combined with the over-relaxation technique and the temperature-exchange method. After performing the MC simulation with finite but low temperature T, we update the state until the energy converges at $T=0$. Consequently, we obtain the stable state at $T=0$, namely, the ground state. We use lattices with periodic boundary conditions (PBCs), containing $L\times L\times 3$ sites, where the maximum number of L is 72.

We calculate order parameters after obtaining the ground state. In the honeycomb lattice, there are several ordered phases. We define the corresponding order parameters in the following.

For the Néel state in the honeycomb lattice (H-Néel), the order parameter is defined as

$$O_{\mathrm{H-N\acute{e}el}}\equiv\frac{1}{(2N)^2}\left|\sum_{l=1}^{N}\left(\mathbf{S}_l^{(1)}-\mathbf{S}_l^{(2)}\right)\right|^2 \tag{11}$$

by using two spins, $\mathbf{S}_l^{(1)}$ and $\mathbf{S}_l^{(2)}$, on the honeycomb sites.

For the stripy state, the order parameter reads

$$O_{\mathrm{stripy}}\equiv\frac{1}{(3N)^2}\left(\left|M_{\mathrm{s}}^{x}\right|^2+\left|M_{\mathrm{s}}^{y}\right|^2+\left|M_{\mathrm{s}}^{z}\right|^2\right), \tag{12}$$

with

$$M_{\mathrm{s}}^{x}=\sum_{l}\sum_{m=1}^{3}S_l^{(m)x}(-1)^{n_1+m},$$

$$M_{\mathrm{s}}^{y}=\sum_{l}\sum_{m=1}^{3}S_l^{(m)y}(-1)^{n_2+m},$$

$$M_{\mathrm{s}}^{z}=\sum_{l}\sum_{m=1}^{3}S_l^{(m)z}(-1)^{n_1+n_2},$$

where n_1 and n_2 specify the position vector at $m=1$ in unit cell l through $\mathbf{r}_l^{(1)}=n_1\mathbf{a}_1+n_2\mathbf{a}_2$. We note that the spin at the central site, $m=3$, inside the honeycomb ring is included in the stripy order parameter.

In the order parameter of the zigzag phase for the honeycomb lattice (H-zigzag), we exclude the $m=3$ site and define

$$O_{\mathrm{H-zigzag}}\equiv\frac{1}{(2N)^2}\left(\left|M_{\mathrm{z}}^{x}\right|^2+\left|M_{\mathrm{z}}^{y}\right|^2+\left|M_{\mathrm{z}}^{z}\right|^2\right), \tag{13}$$

with

$$M_{\mathrm{z}}^{x}=\sum_{l}\sum_{m=1}^{2}S_l^{(m)x}(-1)^{n_1},$$

$$M_{\mathrm{z}}^{y}=\sum_{l}\sum_{m=1}^{2}S_l^{(m)y}(-1)^{n_2},$$

$$M_{\mathrm{z}}^{z}=\sum_{l}\sum_{m=1}^{2}S_l^{(m)z}(-1)^{n_1+n_2+m}.$$

In the triangular lattice, there is a nematic phase whose order parameter is defined as

$$O_{\mathrm{nematic}}\equiv\frac{1}{(3N)^2}\left(\left|M_{\mathrm{n}}^{x}\right|^2+\left|M_{\mathrm{n}}^{y}\right|^2+\left|M_{\mathrm{n}}^{z}\right|^2\right), \tag{14}$$

with

$$\left|M_{\mathrm{n}}^{\gamma}\right|=\sum_{\{\mu_\gamma\}}\left|\sum_{j\in\mu_\gamma}S_j^{\gamma}(-1)^j\right|\quad(\gamma\in\{x,y,z\}),$$

where j runs over all sites in the chain μ_γ connected by the interactions $\mathcal{J}_X$ and $\mathcal{J}_X'$ for $\gamma=x$, $\mathcal{J}_Y$ and $\mathcal{J}_Y'$ for $\gamma=y$, and $\mathcal{J}_Z$ and $\mathcal{J}_Z'$ for $\gamma=z$ (see Fig. 1) and $(-1)^j$ represents alternating signs along the chain. The summation $\{\mu_\gamma\}$ runs over all possible μ_γ chains in the lattice.

The FM order parameter is defined as

$$O_{\mathrm{FM}}\equiv\frac{1}{(3N)^2}\left|\sum_{l=1}^{N}\left(\mathbf{S}_l^{(1)}+\mathbf{S}_l^{(2)}+\mathbf{S}_l^{(3)}\right)\right|^2. \tag{15}$$

C. Exact diagonalization and density-matrix renormalization group

In order to obtain the ground state phase diagram of the Hamiltonian (1) with quantum spins (spin-1/2), we perform the Lanczos-type ED for a 24-site lattice with PBCs, which contains eight unit cells, as depicted in Fig. 1. The lattice is not square in shape but rectangular. To compare ED results with classical ones, we calculate static spin structure factor $S(\mathbf{q})$, defined as

$$S(\mathbf{q})\equiv\sum_{\gamma}S^{\gamma}(\mathbf{q})=\sum_{\gamma}\sum_{m',m}\langle 0|S_{-\mathbf{q}}^{(m')\gamma}S_{\mathbf{q}}^{(m)\gamma}|0\rangle, \tag{16}$$

where $|0\rangle$ represents the ground state.

To check the size dependence of the ground state energy as well as $S(\mathbf{q})$, we perform DMRG calculations for a (12×6)-site system with open boundary conditions along the 12-site direction and PBCs along the 6-site direction, i.e., the cylindrical boundary condition (CBC), where 21 hexagons are involved. In our DMRG, we construct a snakelike one-dimensional chain and use the truncation number $m=1500$, and the resulting

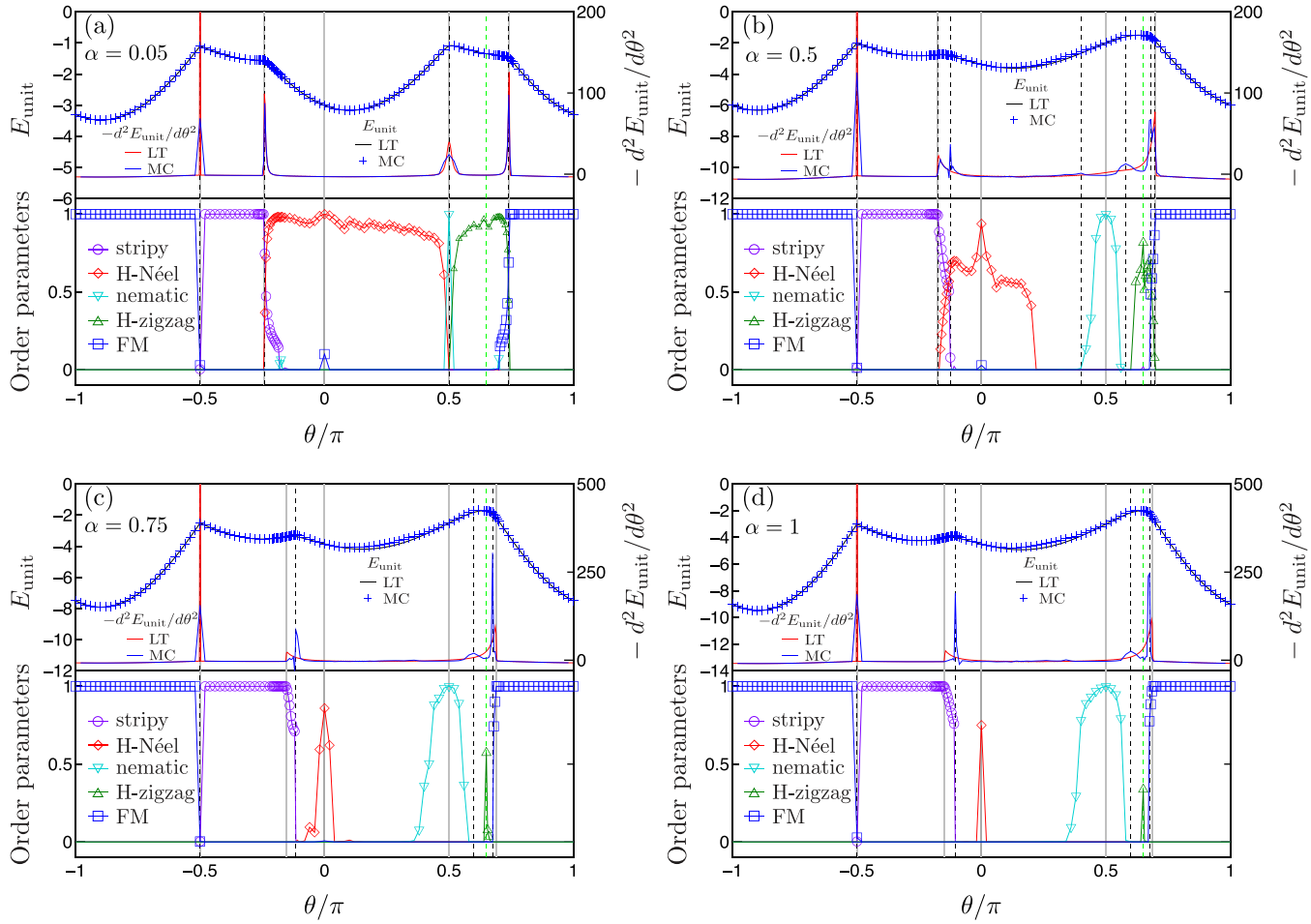

FIG. 2. Classical ground state energy per unit cell $E_{\rm unit}$ and second derivative of $E_{\rm unit}$ with respect to θ, $-d^2E_{\rm unit}/d\theta^2$, obtained by the LT method and the classical MC simulation for a $(72 \times 72 \times 3)$-site lattice with PBCs, together with the order parameters ($O_{\rm stripy}$, $O_{\rm Néel}$, $O_{\rm nematic}$, $O_{\rm H-zigzag}$, and $O_{\rm FM}$) obtained by the classical MC simulation. (a) $\alpha = 0.05$, (b) $\alpha = 0.5$, (c) $\alpha = 0.75$, and (d) $\alpha = 1$. The gray solid vertical lines denote the phase boundaries obtained by the LT method, while the black dashed vertical lines are obtained by the classical MC simulation. The green dashed vertical lines represent the dual point of $\theta = 0$.

truncation error is less than 5×10^{-6}. To compare $S(\mathbf{q})$ from DMRG with that from ED, we use $\mathbf{q}$ values determined by the standard PBCs.

IV. CLASSICAL GROUND STATE PHASE DIAGRAM

We introduce the angle parameter θ that determines the Heisenberg interaction J and the Kitaev interaction K through $J = I_0 \cos\theta$ and $K = I_0 \sin\theta$ [10], where I_0 is the unit of energy, taken to be $I_0 = 1$ in this paper. Changing both θ and α, we construct the phase diagram by examining the ground state energy as well as the order parameters obtained by classical MC simulations.

The ground state energy per unit cell $E_{\rm unit}$, calculated by the LT method and classical MC simulation, and its second derivative, $-d^2E_{\rm unit}/d\theta^2$, are plotted in Fig. 2 as a function of θ for four values of α. We note that $E_{\rm unit}$ at $\alpha = 0^+$ (not shown) and $\alpha = 1$ [Fig. 2(d)] agrees well with previously reported results for the honeycomb and triangular lattices [20,29,30], respectively; for example, in Fig. 2(d), the LT and MC methods give slightly different $E_{\rm unit}$ in the range of $0 < \theta < \pi/2$. This difference comes mainly from the breakdown of the local constraints (5) in the LT method. Therefore, $E_{\rm unit}$ given by the classical MC simulation is more reliable. As a result, the phase boundaries giving rise to singular behaviors in $-d^2E_{\rm unit}/d\theta^2$ are slightly different between the two methods.

At $\alpha = 0.05$, shown in Fig. 2(a), we find four singular points in $-d^2E_{\rm unit}/d\theta^2$. The singularity at the FM Kitaev point $\theta = -\pi/2$ comes from the separation of the FM and stripy phases, which are interrelated by the Klein duality. At $\theta = \pi/2$, on the other hand, the singular behavior is different from that at $\theta = -\pi/2$. In fact, there is nematic order at $\theta = \pi/2$, as shown in the bottom panel. Two other singularities at $\theta \approx -0.25\pi$ and 0.75π are interrelated by the Klein duality and correspond to the first-order transitions from the H-Néel to stripy states and from the H-zigzag to FM states, respectively. We notice that both the H-Néel and stripy orders coexist near $\theta = -0.25\pi$, as shown in the bottom panel. A similar coexisting state occurs near 0.75π between FM and H-zigzag states.

With increasing α, the region of the H-Néel state decreases, while that of the nematic state increases, as evidenced by $O_{\rm Néel}$ and $O_{\rm nematic}$ in Fig. 2. There are no finite order parameters

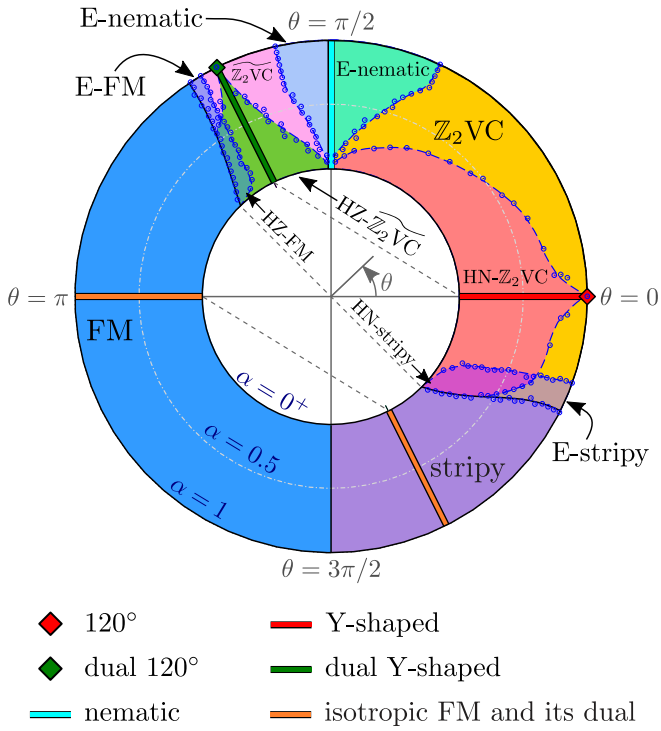

FIG. 3. Classical ground state phase diagram of the KH model parametrized by α and θ. The inner (outer) circle corresponds to $\alpha = 0^+$ ($\alpha = 1$) describing the honeycomb (triangular) lattice. There are various phases, including their dual phases (see the text). The boundaries denoted by the black solid lines are determined by the LT method. The blue dots denote boundaries determined from order parameters calculated by the classical MC simulation for a ($72 \times 72 \times 3$)-site lattice with PBCs. The blue dashed lines interpolate the blue dots. Two θ values inside the circle connected by the dotted lines give the same state due to the Klein duality.

between the H-Néel and nematic states. The boundaries where the H-Néel and nematic order parameters disappear are hard to determine from $-d^2E_{\text{unit}}/d\theta^2$.

The coexisting state of H-Néel and stripy states in Fig. 2(a) clearly persists with increasing α up to $\alpha = 0.5$ near $\theta = -0.14\pi$. With further increasing α, the coexistence disappears, but the reduction of O_{stripy} from 1 is clearly seen at $\theta = -\tan^{-1}(1/2) \sim -0.147\pi$ even for $\alpha = 1$. The reduction indicates the existence of a coexisting state even for $\alpha = 1$. This will be discussed in more detail below.

We show the resulting classical ground state phase diagram in Fig. 3. From the inner circle to the outer circle, α changes from $\alpha = 0^+$ (honeycomb lattice) to $\alpha = 1$ (triangular lattice), and thus, increasing the radius corresponds to increasing α. At $\theta = 0$, a Y-shaped spin state (see below) appears and changes to the so-called 120° state at $\alpha = 1$. Because of the Klein duality [28], a dual Y-shaped spin state and dual 120° state emerge at $\theta = \pi - \tan^{-1} 2$. At $\theta = \pi$, an isotropic FM state appears. At $\theta = \pi/2$, a nematic state appears for $0 < \alpha \leqslant 1$. In addition to these special cases, we identify other phases in Fig. 3: the $\mathbb{Z}_2$VC phase; its dual phase ($\widetilde{\mathbb{Z}_2\text{VC}}$); the extended-nematic phase (E-nematic); the FM phase and its dual phase, called the stripy phase; the extended-stripy (E-stripy) phase; and coexisting phases between H-Néel and $\mathbb{Z}_2$VC (HN-$\mathbb{Z}_2$VC), between H-zigzag and $\widetilde{\mathbb{Z}_2\text{VC}}$ (HZ-$\widetilde{\mathbb{Z}_2\text{VC}}$), between H-zigzag and FM (HZ-FM), and between H-Néel and stripy (HN-stripy).

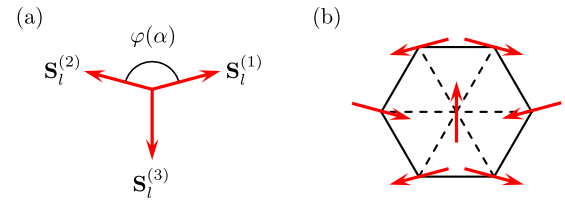

FIG. 4. (a) Y-shaped spin state. The angle φ is given by Eq. (17). (b) Snapshot of the ground state stabilized at $J = 1$ and $K = 0$. The ratio of interactions between the solid and dashed bonds is $1 : \alpha$.

We will discuss the characteristic behaviors of several phases.

A. Y-shaped spin state and 120° state

At $\theta = 0$, i.e., $(J, K) = (1, 0)$, the model becomes the antiferromagnetic Heisenberg model. The three spins in the unit cell form a Y shape, as shown in Fig. 4(a), where the angle between $\mathbf{S}_l^{(1)}$ and $\mathbf{S}_l^{(2)}$ is given by

$$\varphi(\alpha) = \cos^{-1}\left(-1 + \frac{\alpha^2}{2}\right). \tag{17}$$

The φ becomes π for the honeycomb limit ($\alpha = 0^+$) and $2\pi/3 = 120°$ for the triangular lattice ($\alpha = 1$). The ground state becomes a coplanar state with three sublattices, as shown in Fig. 4(b), where $E_{\text{unit}} = -3(1 + \frac{\alpha^2}{2})I_0$.

The ground state at $\theta = 0$ has degeneracy characterized by the order parameter space SO(3) due to geometrical frustration, as is the case for the triangular lattice, and thus, the first homotopy group is given by $\pi_1(\text{SO}(3)) = \mathbb{Z}_2$ [40,41]. Therefore, similar to the previous study on the triangular lattice [29,30,35], a $\mathbb{Z}_2$ vortex crystal phase is expected in our model when the Kitaev interaction is finite ($K \neq 0$).

For frustrated spin systems such as the triangular Heisenberg model ($\alpha = 1$ and $\theta = 0$), vector chirality is a good quantity to characterize frustration [41]. We define the vector chirality at site i as

$$\boldsymbol{\kappa}_i \equiv \frac{2}{\sqrt{(2-\alpha)(\alpha+2)^3}}\left(\mathbf{S}_i \times \mathbf{S}_j + \mathbf{S}_j \times \mathbf{S}_k + \mathbf{S}_k \times \mathbf{S}_i\right), \tag{18}$$

where site j (k) is the nearest-neighbor site of i with the displacement vector $(\mathbf{a}_1 + \mathbf{a}_2)/3$ $[(-\mathbf{a}_1 + 2\mathbf{a}_2)/3]$ from i and thus the three sites, i, j, and k, form a triangle. The prefactor in Eq. (18) is chosen for the Y-shaped spin state to be $|\boldsymbol{\kappa}_i| = 1$. We note that $\boldsymbol{\kappa}_i$ is aligned in the same direction independent of site i.

The Klein duality gives dual 120° and dual Y-shaped states, as shown in Fig. 3.

B. $\mathbb{Z}_2$VC phase

Away from $\theta = 0$ and close to $\alpha = 1$, the $\mathbb{Z}_2$VC phase spreads in the region of $-0.1\pi \lesssim \theta \lesssim 0.4\pi$. In order to demonstrate the presence of vortices, we calculate the vector

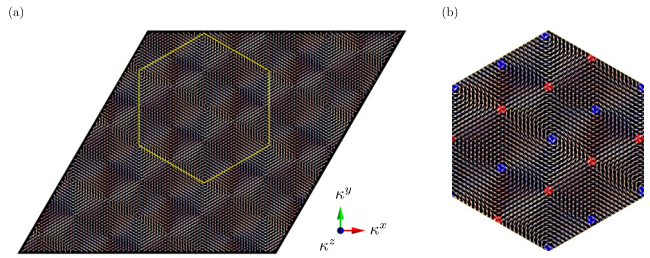

FIG. 5. (a) Snapshot of vector chirality $\boldsymbol{\kappa}_i$ in the $\mathbb{Z}_2$VC phase of a $(48 \times 48 \times 3)$-site lattice with PBCs obtained by the classical MC simulation. $\alpha = 0.96$ and $\theta = -0.08\pi$. An arrow on each site represents $\boldsymbol{\kappa}_i$ projected onto the κ^x-κ^y plane. (b) Enlarged view of $\boldsymbol{\kappa}_i$ in the area surrounded by yellow lines in (a). The blue (red) dots denote the center of vortices (antivortices), which forms a crystal.

chirality $\boldsymbol{\kappa}_i$ at $\alpha = 0.96$ and $\theta = -0.08\pi$, which is shown in Fig. 5 for an $N = 48 \times 48 \times 3$ site lattice with PBCs. Vortices and antivortices appear in pairs: the vortices are centered at the blue dots, while the antivortices are at the red dots in Fig. 5(b). Since there is translational invariance, the vortex-antivortex pairs form a crystal. The averaged magnitude of the vector chirality given by $N^{-1}\sum_i |\boldsymbol{\kappa}_i|$ is 0.99, which is close to 1, implying that spins locally tend to form the Y-shaped ordering. The main reason that the average value deviates from the ideal value of 1 is the distortion of the spin configuration from the Y shape around the cores. Thus, the cores of the $\mathbb{Z}_2$ vortices appear as the defects of the Y-shaped spin state. Like in the case of the triangular lattice [30], the distance between the vortex cores becomes shorter as $|K|$ becomes larger.

The Klein duality gives the dual-$\mathbb{Z}_2$VC phase that is denoted as $\widetilde{\mathbb{Z}_2\text{VC}}$ in Fig. 3.

C. HN-$\mathbb{Z}_2$VC phase

With decreasing α in the $\mathbb{Z}_2$VC phase, the H-Néel order emerges at a critical value of α. In spite of the presence of the H-Néel order, the vortex-antivortex pairs remain. Therefore, we call the coexisting phase the HN-$\mathbb{Z}_2$VC phase.

To confirm the coexistence of the H-Néel order and the $\mathbb{Z}_2$VC, we show $\mathbf{S}(\mathbf{q})$ obtained by the classical MC simulation for a $(48 \times 48 \times 3)$-site periodic lattice with $\theta = 0.2\pi$ and $\alpha = 0.2$ in Figs. 6(a)–6(c). $S^z(\mathbf{q})$ in Fig. 6(c) clearly shows strong intensity at the corner of the Brillouin zone, consistent with the H-Néel state. $S^x(\mathbf{q})$ in Fig. 6(a) and $S^y(\mathbf{q})$ in Fig. 6(b) exhibit strong intensity slightly away from the corner, which is consistent with the signature of $\mathbb{Z}_2$VC discussed in the triangular lattice [29]. In addition, we find two incommensurate structures around $\mathbf{q} = (0, 0)$ in both $S^x(\mathbf{q})$ and $S^y(\mathbf{q})$. This is due to the remnants of FM order at $\theta = 0$ seen in Figs. 2(a) and 2(b), which are shifted to finite $\mathbf{q}$ by the presence of $\mathbb{Z}_2$VC.

As α decreases, the distance between the vortex and antivortex increases, accompanied by the reduction in the magnitude of $\boldsymbol{\kappa}_i$. At $\alpha = 0^+$, the Néel phase on the honeycomb lattice appears [6,7,10].

The H-Néel state is changed to H-zigzag by the Klein duality. Therefore, the HN-$\mathbb{Z}_2$VC phase corresponds to the HZ-$\widetilde{\mathbb{Z}_2\text{VC}}$ phase in Fig. 3.

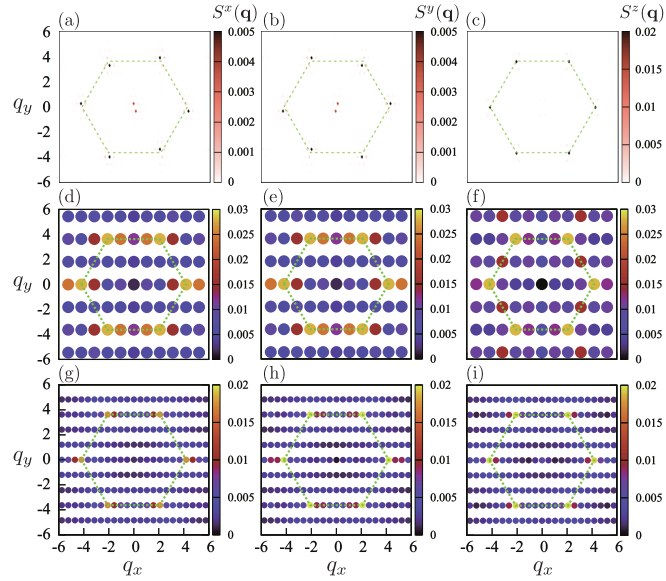

FIG. 6. Ground state spin structure factor in the HN-$\mathbb{Z}_2$VC phase in the extended Brillouin zone. $\theta = 0.2\pi$ and $\alpha = 0.2$. (a) $S^x(\mathbf{q})$, (b) $S^y(\mathbf{q})$, and (c) $S^z(\mathbf{q})$ in the classical system with a $(48 \times 48 \times 3)$-site lattice, obtained by the classical MC simulation at $T = 0$. (d) $S^x(\mathbf{q})$, (e) $S^y(\mathbf{q})$, and (f) $S^z(\mathbf{q})$ in the quantum system with a 24-site lattice, obtained by the ED method. The circles denote the momentum positions defined in the lattice. (g) $S^x(\mathbf{q})$, (h) $S^y(\mathbf{q})$, and (i) $S^z(\mathbf{q})$ in the quantum system with a (12×6)-site lattice, obtained by the DMRG method. The circles denote the momentum positions defined by assuming PBCs for the lattice. The green dotted hexagon in each panel represents the first Brillouin zone of the triangular lattice.

D. Nematic phase

At $\theta = \pi/2$, i.e., $(J, K) = (0, 1)$, the Hamiltonian (1) becomes the Kitaev model. In the triangular lattice ($\alpha = 1$), a nematic state appears [29,30,35]. Even for $0 < \alpha < 1$, we find the same nematic state using the LT method with $E_{\text{unit}} = -(1 + 2\alpha)I_0$. In this phase, the spin configuration is given by

$$\mathbf{S}_l^{(m)} = \begin{pmatrix} f^x_{n_1+2n_2+m} & (-1)^{n_2+m} \\ f^y_{2n_1+n_2+m} & (-1)^{n_1+m} \\ f^z_{-n_1+n_2} & (-1)^{n_1+m} \end{pmatrix}, \tag{19}$$

where the sets $\{f^x_{n_1+2n_2+m}\}$, $\{f^y_{2n_1+n_2+m}\}$, and $\{f^z_{-n_1+n_2}\}$ have arbitrary numbers under the local constraints (5). Therefore, in the classical level, the model has subextensive ground state degeneracy, as discussed by Rousochatzakis *et al.* [30]. Figure 7(a) shows one of the spin configurations for the set of parameters listed in the caption, where lines connected by blue solid and dotted line segments denote the μ_z chains. We note that the γ ($\gamma = x$, y, and z) component of the spins in the nematic phase aligns antiferromagnetically along the μ_γ chain. Thus, each direction leads to 2^L-fold states, where L is the linear system size. The degenerate ground states are given by $\mathbf{q}'$ in the first Brillouin zone shown in Fig. 7(b). One of the three directions becomes lower in free energy by, for example, thermal fluctuation, leading to the nematic state [30].

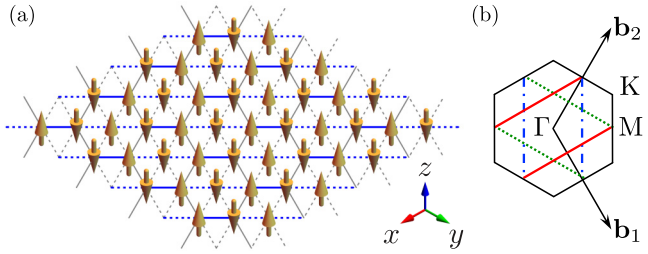

FIG. 7. (a) One of the spin configurations at the (3×2^L)-fold degenerated nematic phase at $\theta = \pi/2$, obtained by the LT method for a $(4 \times 4 \times 3)$-site lattice. The parameters in Eq. (19) are set to $f^x_{n_1+2n_2+m} = 0$, $f^y_{2n_1+n_2+m} = 0$, $f^z_0 = -1$, $f^z_1 = 1$, $f^z_2 = 1$, and $f^z_3 = -1$. (b) Wave numbers $\mathbf{q}'$ that give the degenerate ground states in the nematic phase in the first Brillouin zone. The red solid, green dotted, and blue dash-dotted lines represent $(\mathbf{q}', x)$, $(\mathbf{q}', y)$, and $(\mathbf{q}', z)$, respectively. $\mathbf{b}_1$ and $\mathbf{b}_2$ are two primitive translation vectors of the reciprocal lattice.

E. E-nematic phase

The nematic order parameter $O_{\rm n}$ in (14) calculated by the classical MC simulation is not unity but finite across $\theta = \pi/2$ for $0 < \alpha \leqslant 1$ (see Fig. 2). We call this phase the extended-nematic phase. This E-nematic phase narrows with the decrease of α and converges to a single point at $\alpha = 0^+$.

$\mathbf{S}(\mathbf{q})$ is shown in Fig. 8 for $\theta = 0.45\pi$ and $\alpha = 0.8$. All of the x, y, and z components have a two-line structure with nonuniform intensity, but the z component is different from the x and y components. The two-line structure exhibits nematic behavior but not a perfect nematic state characterized by uniform lines as expected from Fig. 7(b). This is nothing but the remnants of the perfect nematic state.

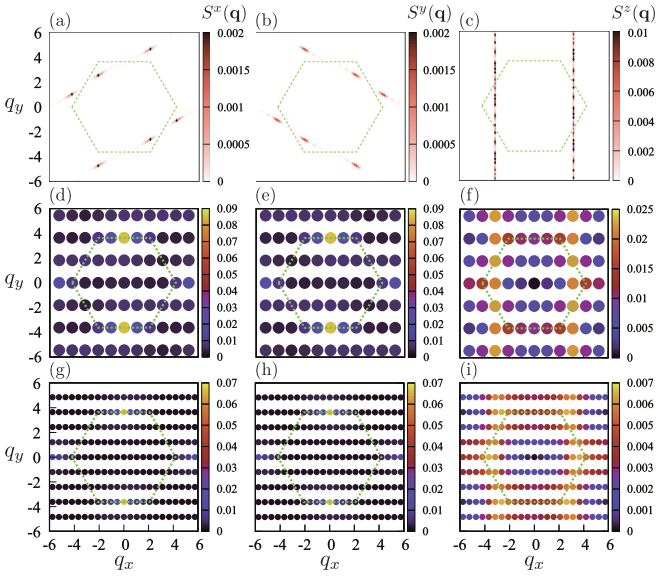

FIG. 8. The same as Fig. 6, but in the E-nematic phase. $\theta = 0.45\pi$ and $\alpha = 0.8$.

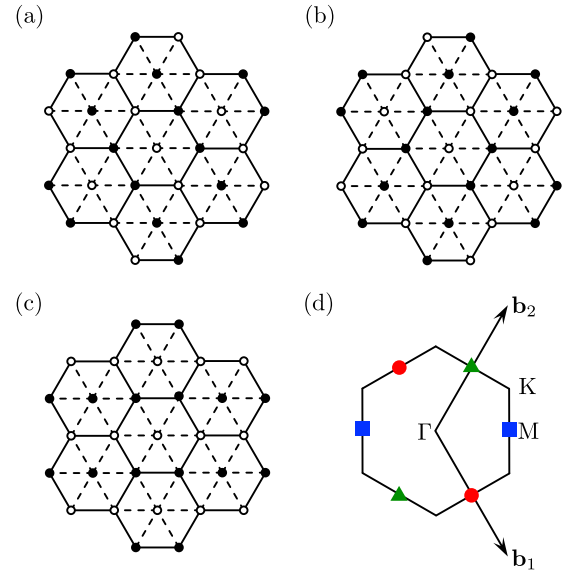

FIG. 9. Schematic view of spin arrangement in the stripy phase obtained by the LT method. (a) x component of spin S^x_i, (b) y component of spin S^y_i, and (c) z component of spin S^z_i. The solid and open circles represent opposite signs of S^γ_i. The ratio of interactions between the solid and dashed bonds is $1 : \alpha$. (d) Wave numbers $\mathbf{q}'$ giving the ground state in the first Brillouin zone. The red circles, green triangles, and blue squares represent $(\mathbf{q}', x)$, $(\mathbf{q}', y)$, and $(\mathbf{q}', z)$, respectively. All of these $\mathbf{q}'$ are on the M points. $\mathbf{b}_1$ and $\mathbf{b}_2$ are two primitive translation vectors of the reciprocal lattice.

F. Stripy, E-stripy, and HN-stripy phases

The stripy phase has been discussed in the honeycomb lattice [6,10,20] as well as in the triangular lattice as the dual-FM phase [28–31,35]. The LT method gives the ground state with $E_{\rm unit} = -(1 + 2\alpha)(J - K)$ at the M points shown in Fig. 9(d). These wave numbers lead to the spin configuration given by

$$\mathbf{S}^{(m)}_l = \begin{pmatrix} f^x & (-1)^{n_1+m} \\ f^y & (-1)^{n_2+m} \\ f^z & (-1)^{n_1+n_2} \end{pmatrix}, \tag{20}$$

where f^x, f^y, and f^z satisfy $(f^x)^2 + (f^y)^2 + (f^z)^2 = 1$ by the local constraints (5). Thus, in the classical level, the order parameter space is S^2. The schematic view of spin arrangement is shown in Figs. 9(a), 9(b), and 9(c) for the x, y, and z components of spin, respectively, where the FM arrangement appears along the bond of the γ components of the Kitaev interaction, forming a stripe shape of spin distribution.

The stripy phase is the dual phase of the FM phase through the Klein duality. Namely, $\theta = -\tan^{-1} 2$ in the stripy phase corresponds to the pure FM Heisenberg model at $\theta = \pi$, which is represented by the orange line in Fig. 3. Therefore, the stripy state at $\theta = -\tan^{-1} 2$ is the ground state even for quantum spins. When $\theta \neq -\tan^{-1} 2$, there is the possibility that some degeneracy can be lifted by the order-by-disorder mechanism because the corresponding Hamiltonian is not SU(2) symmetric. Indeed, it has been pointed out that spins lie along one of the cubic axes on the triangular lattice [29,30].

The stripy order parameter O_{stripy} in (12) changes from 1 to a smaller value when θ approaches zero [see Figs. 2(c) and 2(d)], forming a coexisting phase with $\mathbb{Z}_2$VC. We call this coexisting phase the extended-stripy phase. The distance between the vortex and antivortex becomes smaller when approaching the stripy phase from $\mathbb{Z}_2$VC. Because of the finite size of the vortices, the stripy order parameter becomes finite before the vortex-antivortex pair diminishes. This might be the origin of the coexisting phase. The dual phase of E-stripy is E-FM.

O_{stripy} also coexists with $O_{\text{H-Néel}}$, as shown in Figs. 2(a) and 2(b). Therefore, we call this region the HN-stripy phase, whose dual phase is HZ-FM, as shown in Fig. 3.

V. QUANTUM GROUND STATE PHASE DIAGRAM

In order to construct a quantum-mechanical phase diagram of the honeycomb-triangular KH model (1), we calculate the ground state energy using the ED method for the 24-site lattice. Figure 10 shows E_{unit} as a function of α and the second derivative with respect to α, $-d^2E_{\text{unit}}/d\alpha^2$, for given θ. To check the size dependence, we also show E_{unit} by DMRG for the (12×6)-site lattice with the CBC in Fig. 10. The ED and DMRG results for E_{unit} show α dependences similar to each other. The second derivative of E_{unit} at $\theta = 0.2\pi$ shown in Fig. 10(a) exhibits two anomalies around $\alpha = 0.5$ in ED but not in DMRG. The anomalies come from level crossing due to small system size. However, their positions as well as the broad maximum in the DMRG result are closely located at the classical phase boundary denoted by α_{C} in Fig. 10(a). Therefore, a phase boundary is expected to exist near the classical one. The results at $\theta = 0.45\pi$ shown in Fig. 10(b) also exhibit a possible phase boundary close to the classical one denoted by α_{C1}, although the anomaly around α_{C2} is unclear.

Taking into account the second derivative of E_{unit} as well as $\mathbf{S}(\mathbf{q})$ (not shown), we construct a phase diagram using the ED method, as shown in Fig. 11. The phase boundaries are drowned by interpolating some of the points that indicate the change in phases. We can recognize similarity to the classical phase diagram in Fig. 3 at a glance.

However, there are several differences between the two phase diagrams. The most prominent difference is a complicated distribution of many phases around the region of $\alpha \sim 0.5$ and $-0.2\pi \lesssim \theta \lesssim 0.25\pi$ together with its dual region. Along the $\theta = 0$ line, the total spin of the system changes from zero at $\alpha = 1$ to discreet finite values with decreasing α, with a return to zero for $\alpha < 0.32$. Those states with finite total spin at $\theta = 0$ are smoothly connected to the phases showing the complicated distribution. Another difference between the classical and quantum phase diagrams appears at the E-nematic phase. In the classical case, the boundary separating the E-nematic and $\mathbb{Z}_2$VC phases reaches the Kitaev spin liquid point, i.e., $\theta = \pi/2$ and $\alpha = 0$. In contrast, the boundary in the quantum case extends toward smaller θ starting from $\theta \sim 0.4\pi$ at $\alpha = 1$. However, we find a point along the boundary where the transition changes from a weakly first-order type to a second-order type. Therefore, we expect a possible point where the character of the boundary changes, and thus, we draw the dashed line from the possible point to the Kitaev spin-liquid point. Of course, the phase diagram obtained by ED suffers from the finite-size effect. DMRG would be a possible alternative method, but unfortunately, the numerical costs to make a complete phase diagram are demanding. Making the complete phase diagram in the quantum system remains a future problem.

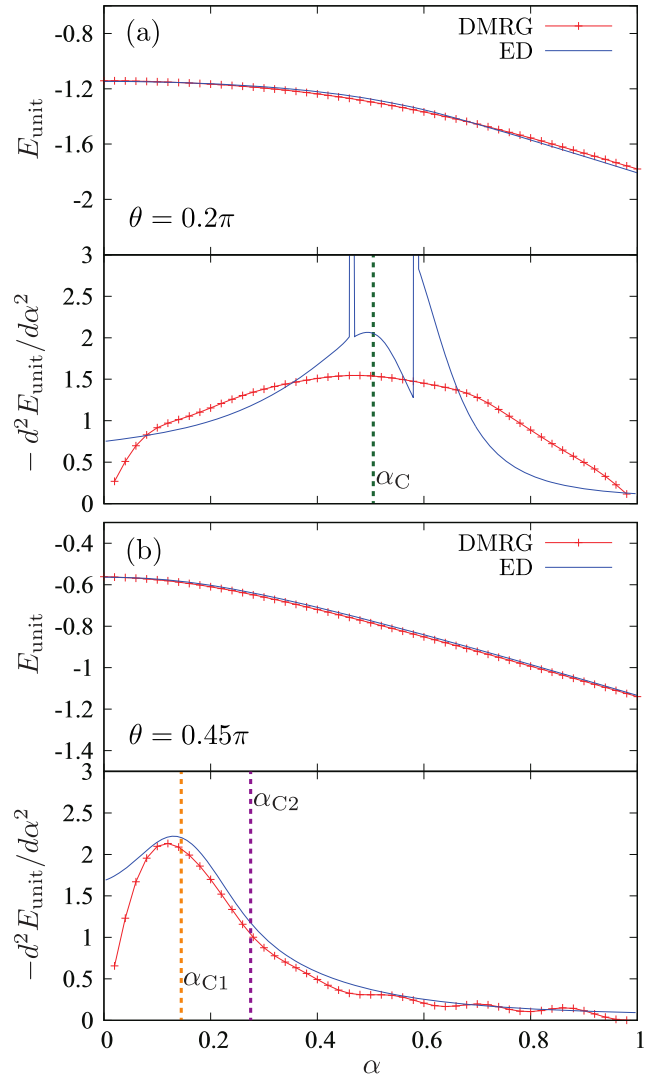

FIG. 10. Quantum ground state energy per unit cell E_{unit} and second derivative of E_{unit} with respect to α, $-d^2E_{\text{unit}}/d\alpha^2$, obtained by the ED method for a 24-site lattice and by DMRG for a (12×6)-site lattice. (a) $\theta = 0.2\pi$ and (b) $\theta = 0.45\pi$. The vertical dotted lines correspond to phase boundaries obtained by the classical MC simulations.

We also examine $\mathbf{S}(\mathbf{q})$ using the ED and DMRG methods and compare them with the classical results. Figures 6 and 8 show $\mathbf{S}(\mathbf{q})$ in the HN-$\mathbb{Z}_2$VC and E-nematic phases, respectively. The ED and DMRG results are similar to each other, indicating small system-size dependence. In the E-nematic phase, we find a $\mathbf{q}$ direction with large intensity in $S^z(\mathbf{q})$ [see Figs. 8(f) and 8(i)], which is qualitatively consistent with the classical one in Fig. 8(c). This means that both the quantum and classical systems have the same E-nematic phase. The ED results of $S^x(\mathbf{q})$ in Fig. 8(d) and $S^y(\mathbf{q})$ in Fig. 8(e) show the same behavior. The DMRG results in Figs. 8(g) and 8(h) are

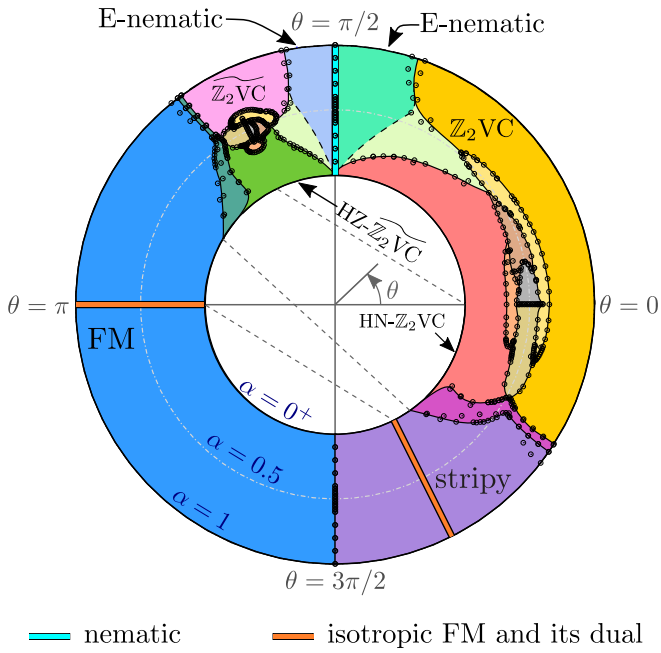

FIG. 11. Quantum ground state phase diagram of the KH model parametrized by α and θ, obtained by the ED method for a 24-site lattice with PBCs. The inner (outer) circle corresponds to $\alpha = 0^+$ ($\alpha = 1$) describing the honeycomb (triangular) lattice. There are various phases, including their dual phases, similar to the classical phase diagram shown in Fig. 3. The phases appearing in Fig. 3 are depicted by the same color as in Fig. 3. The other phases that do not appear in Fig. 3 are due to the finite-size effect. Two values of θ inside the circle connected by the dotted lines give the same state as a result of the Klein duality.

also similar. These similarities, however, are not seen in the classical results in Figs. 8(a) and 8(b). The difference indicates that the degeneracy between $S^x(\mathbf{q})$ and $S^y(\mathbf{q})$ is not lifted in quantum systems. In the HN-$\mathbb{Z}_2$VC phase, the HN feature is clearly seen, as evidenced by strong intensity at the corner of the Brillouin zone in $S^z(\mathbf{q})$ [see Figs. 6(f) and 6(i)], consistent with the classical case in Fig. 6(c). However, the evidence of $\mathbb{Z}_2$VC is unclear because the intensity of $S^x(\mathbf{q})$ in Figs. 6(d) and 6(g) as well as that of $S^y(\mathbf{q})$ in Figs. 6(e) and 6(h) is distributed differently from the classical ones. This is probably due to small system size along the y direction in quantum cases.

VI. SUMMARY

In summary, we constructed a model connecting the honeycomb and triangular KH lattices and examined the ground state of the classical system using the LT method and the classical MC simulation. We found coexisting phases in the honeycomb-triangular lattice which are composed of known phases in the honeycomb and triangular lattices. The quantum effects on the honeycomb-triangular lattice were examined using the ED and DMRG methods. The phase boundaries in the classical phase were suggested to survive even though quantum fluctuations were introduced, as demonstrated by the phase diagram obtained by the ED method. However, the quantum phase diagram suffers from the finite-size effect. Therefore, it is desired to perform a systematic study increasing the system size, which remains a future problem.

There is, unfortunately, no real material corresponding to our model at present. However, we expect that such materials are realizable by distorting the lattice or replacing the magnetic ions with others in the possible materials described by the triangular KH model. In fact, recently, we became aware of new materials close to our honeycomb-triangular structure, $CsFe_3(SeO_3)_2F_6$ [42] and $TbInO_3$ [43], although these materials do not seem to have Kitaev-type interactions. These syntheses of honeycomb-triangular materials encourage us to investigate our model, and we expect that materials corresponding to our model will be synthesized in the near future.

ACKNOWLEDGMENTS

We thank K. Shinjo, Y. Yamaji, T. Okubo, T. Suzuki, N. Kawashima, and M. Imada for useful discussions. This work was supported by MEXT, Japan, as a social and scientific priority issue (creation of new functional devices and high-performance materials to support next-generation industries) to be tackled by using a post-K computer. This work partly used computational resources of the K computer provided by the RIKEN Center for Computational Science through the HPCI System Research project (Projects No. hp140136, No. hp150142, and No. hp160122). This work has also been supported by a Grant-in-Aid for Scientific Research from MEXT, Japan, under Grant No. 17K14148. The numerical calculation was carried out at the K Computer and HOKUSAI, RIKEN Center for Computational Science, and the facilities of the Supercomputer Center, Institute for Solid State Physics, University of Tokyo.

[1] G. Jackeli and G. Khaliullin, Phys. Rev. Lett. **102**, 017205 (2009).
[2] K. Kugel and D. Khomskii, Sov. Phys. Usp. **25**, 231 (1982).
[3] G. Khaliullin, Prog. Theor. Phys. Suppl. **160**, 155 (2005).
[4] For a review see Z. Nussinov and J. van den Brink, Rev. Mod. Phys. **87**, 1 (2015).
[5] A. Kitaev, Ann. Phys. (NY) **321**, 2 (2006).
[6] J. Chaloupka, G. Jackeli, and G. Khaliullin, Phys. Rev. Lett. **105**, 027204 (2010).
[7] H.-C. Jiang, Z.-C. Gu, X.-L. Qi, and S. Trebst, Phys. Rev. B **83**, 245104 (2011).
[8] J. Reuther, R. Thomale, and S. Trebst, Phys. Rev. B **84**, 100406 (2011).
[9] R. Schaffer, S. Bhattacharjee, and Y. B. Kim, Phys. Rev. B **86**, 224417 (2012).
[10] J. Chaloupka, G. Jackeli, and G. Khaliullin, Phys. Rev. Lett. **110**, 097204 (2013).
[11] S. Okamoto, Phys. Rev. B **87**, 064508 (2013).
[12] C. Price and N. B. Perkins, Phys. Rev. B **88**, 024410 (2013).
[13] E. Sela, H.-C. Jiang, M. H. Gerlach, and S. Trebst, Phys. Rev. B **90**, 035113 (2014).
[14] I. Kimchi and Y.-Z. You, Phys. Rev. B **84**, 180407 (2011).

[15] Y. Singh, S. Manni, J. Reuther, T. Berlijn, R. Thomale, W. Ku, S. Trebst, and P. Gegenwart, Phys. Rev. Lett. **108**, 127203 (2012).
[16] S. K. Choi, R. Coldea, A. N. Kolmogorov, T. Lancaster, I. I. Mazin, S. J. Blundell, P. G. Radaelli, Y. Singh, P. Gegenwart, K. R. Choi, S.-W. Cheong, P. J. Baker, C. Stock, and J. Taylor, Phys. Rev. Lett. **108**, 127204 (2012).
[17] J. Reuther, R. Thomale, and S. Rachel, Phys. Rev. B **90**, 100405(R) (2014).
[18] S. Bhattacharjee, S.-S. Lee, and Y. B. Kim, New J. Phys. **14**, 073015 (2012).
[19] V. M. Katukuri, S. Nishimoto, V. Yushankhai, A. Stoyanova, H. Kandpal, S. Choi, R. Coldea, I. Rousochatzakis, L. Hozoi, and J. van den Brink, New J. Phys. **16**, 013056 (2014).
[20] J. G. Rau, E. K.-H. Lee, and H.-Y. Kee, Phys. Rev. Lett. **112**, 077204 (2014).
[21] J. G. Rau and H.-Y. Kee, arXiv:1408.4811.
[22] Y. Yamaji, Y. Nomura, M. Kurita, R. Arita, and M. Imada, Phys. Rev. Lett. **113**, 107201 (2014).
[23] Y. Sizyuk, C. Price, P. Wölfle, and N. B. Perkins, Phys. Rev. B **90**, 155126 (2014).
[24] I. Kimchi, R. Coldea, and A. Vishwanath, Phys. Rev. B **91**, 245134 (2015).
[25] K. Shinjo, S. Sota, and T. Tohyama, Phys. Rev. B **91**, 054401 (2015).
[26] J. Chaloupka and G. Khaliullin, Phys. Rev. B **92**, 024413 (2015).
[27] T. Okubo, K. Shinjo, Y. Yamaji, N. Kawashima, S. Sota, T. Tohyama, and M. Imada, Phys. Rev. B **96**, 054434 (2017).
[28] I. Kimchi and A. Vishwanath, Phys. Rev. B **89**, 014414 (2014).
[29] M. Becker, M. Hermanns, B. Bauer, M. Garst, and S. Trebst, Phys. Rev. B **91**, 155135 (2015).
[30] I. Rousochatzakis, U. K. Rossler, J. van den Brink, and M. Daghofer, Phys. Rev. B **93**, 104417 (2016).
[31] K. Li, S.-L. Yu, and J.-X. Li, New J. Phys. **17**, 043032 (2015).
[32] K. Shinjo, S. Sota, S. Yunoki, K. Totsuka, and T. Tohyama, J. Phys. Soc. Jpn. **85**, 114710 (2016).
[33] T. Dey, A. V. Mahajan, P. Khuntia, M. Baenitz, B. Koteswararao, and F. C. Chou, Phys. Rev. B **86**, 140405(R) (2012).
[34] W.-J. Lee, S.-H. Do, S. Yoon, S. Lee, Y. S. Choi, D. J. Jang, M. Brando, M. Lee, E. S. Choi, S. Ji, Z. H. Jang, B. J. Suh, and K.-Y. Choi, Phys. Rev. B **96**, 014432 (2017).
[35] A. Catuneanu, J. G. Rau, H.-S. Kim, and H.-Y. Kee, Phys. Rev. B **92**, 165108 (2015).
[36] J. M. Luttinger and L. Tisza, Phys. Rev. **70**, 954 (1946).
[37] D. B. Litvin, Physica (Amsterdam) **77**, 205 (1974).
[38] A. Yoshimori, J. Phys. Soc. Jpn. **14**, 807 (1959).
[39] M. J. Freiser, Phys. Rev. **123**, 2003 (1961).
[40] N. D. Mermin, Rev. Mod. Phys. **51**, 591 (1979).
[41] H. Kawamura and S. Miyashita, J. Phys. Soc. Jpn. **53**, 4138 (1984).
[42] H. Lu and H. Kageyama, Inorg. Chem. **57**, 6186 (2018).
[43] L. Clark, G. Sala, D. D. Maharaj, M. B. Stone, K. S. Knight, M. T. F. Telling, X. Wang, X. Xu, J. Kim, Y. Li, S.-W. Cheong, and B. D. Gaulin, arXiv:1806.08215.